ACS APPLIED ELECTRONIC MATERIALS

pubs.acs.org/acsaelm Article

Electroforming-Free HfO_2:CeO_2 Vertically Aligned Nanocomposite Memristors with Anisotropic Dielectric Response

Hongyi Dou, Xingyao Gao, Di Zhang, Samyak Dhole, Zhimin Qi, Bo Yang, Md Nazmul Hasan, Jung-Hun Seo, Quanxi Jia, Markus Hellenbrand, Judith L. MacManus-Driscoll, Xinghang Zhang, and Haiyan Wang*

Cite This: *ACS Appl. Electron. Mater.* 2021, 3, 5278−5286 Read Online

ACCESS | Metrics & More | Article Recommendations | Supporting Information

ABSTRACT: Resistive switching and anisotropic optical properties have been investigated in two-phase HfO_2:CeO_2 nanocomposite thin films of different HfO_2:CeO_2 ratios of 3:1, 1:1, and 1:3 on single-crystalline $SrTiO_3$(001) substrates. Vertically aligned nanocomposite (VAN) thin films with CeO_2 pillars embedded in a HfO_2 matrix have been obtained using a one-step pulsed laser deposition technique. By adjusting the molar ratio of HfO_2 and CeO_2 in the films, the resistive switching effect and the anisotropic dielectric response were tuned and correlated with the density of the conducting vertical-phase boundaries. It is shown that only HfO_2:CeO_2 VAN films of 1:1 composition give rise to a forming-free switching system as they have clear vertical boundaries that guide oxygen vacancy channels. These films show strong promise for resistive switching memory devices.

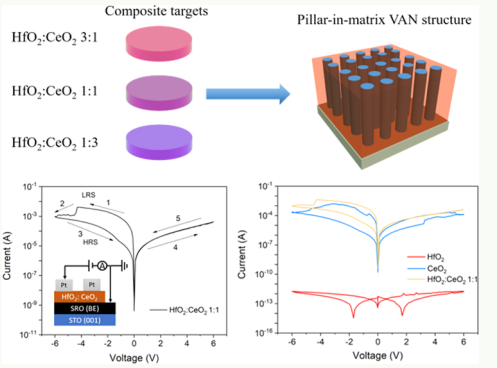

KEYWORDS: *HfO_2, CeO_2, vertically aligned nanocomposite (VAN), electroforming free, resistive switching, oxygen vacancies, anisotropy*

INTRODUCTION

As the miniaturizing limit of the traditional memory quickly approaches, resistive random-access memory (RRAM) has shown strong promise owing to simple compositions, relatively fast switching, as well as good endurance and retention. The most commonly accepted resistive switching mechanism is the filamentary switching. In filamentary switching, the change in resistance arises from the growth and rupture of localized conduction filaments, usually composed of oxygen vacancies, through the insulating layer.[1] However, the irreversible electroforming process, which is often required to activate the filamentary RRAM devices, has become a major problem in achieving scaling, and low-power-consumption memory devices. Thus, an electroforming-free RRAM device is highly desired.

Typical materials using RRAM as the insulating layer are mainly metal oxides,[2] including $SrTiO_3$,[3−6] TiO_2,[7−10] Ta_2O_5,[11,11] VO_2,[12,12] NiO,[13,14] HfO_2,[15−19,15−19] CeO_2,[20−25,20−25] etc. HfO_2 and CeO_2 are popular candidates for the following reasons: (1) both are high-k materials that have been investigated to a great extent due to their simple structure and high compatibility with CMOS integrated circuits; (2) RRAM devices based on HfO_2 have been reported to excel in several aspects, including R_{HRS}/R_{LRS} ratio, endurance, and retention;[26] (3) CeO_2 draws increasing attention due to its intriguing features: fast generation and elimination of oxygen vacancies through reversible valence changes between Ce^{4+} and Ce^{3+} and high oxygen ion/vacancy conductivity.[27,28]

For most of the investigated oxide-based RRAM devices, current challenges in improving the scalability, uniformity, and retention are related to control over oxygen ion/vacancy density, location, and mobility. Defects such as dislocations and grain boundaries have previously been reported to be conductive channels and preferential sites for oxygen vacancy accumulation in oxide-based RRAM devices,[5,29] and can improve the RRAM performance by controlling the formation and rupture of conducting filaments. However, most oxides, including polycrystalline or amorphous insulating HfO_2 and CeO_2, result in the random generation of conducting filaments, which hamper the uniformity and scalability of the devices, as well as lead to high energy consumption from the electroforming process.

Tackle the aforementioned challenges, highly oriented grain boundaries[30] or phase boundaries are desirable. Vertically aligned nanocomposites (VAN), in which two non-miscible materials can form a two-phase system with either pillar−pillar

Received: August 27, 2021
Accepted: November 9, 2021
Published: November 20, 2021

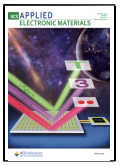

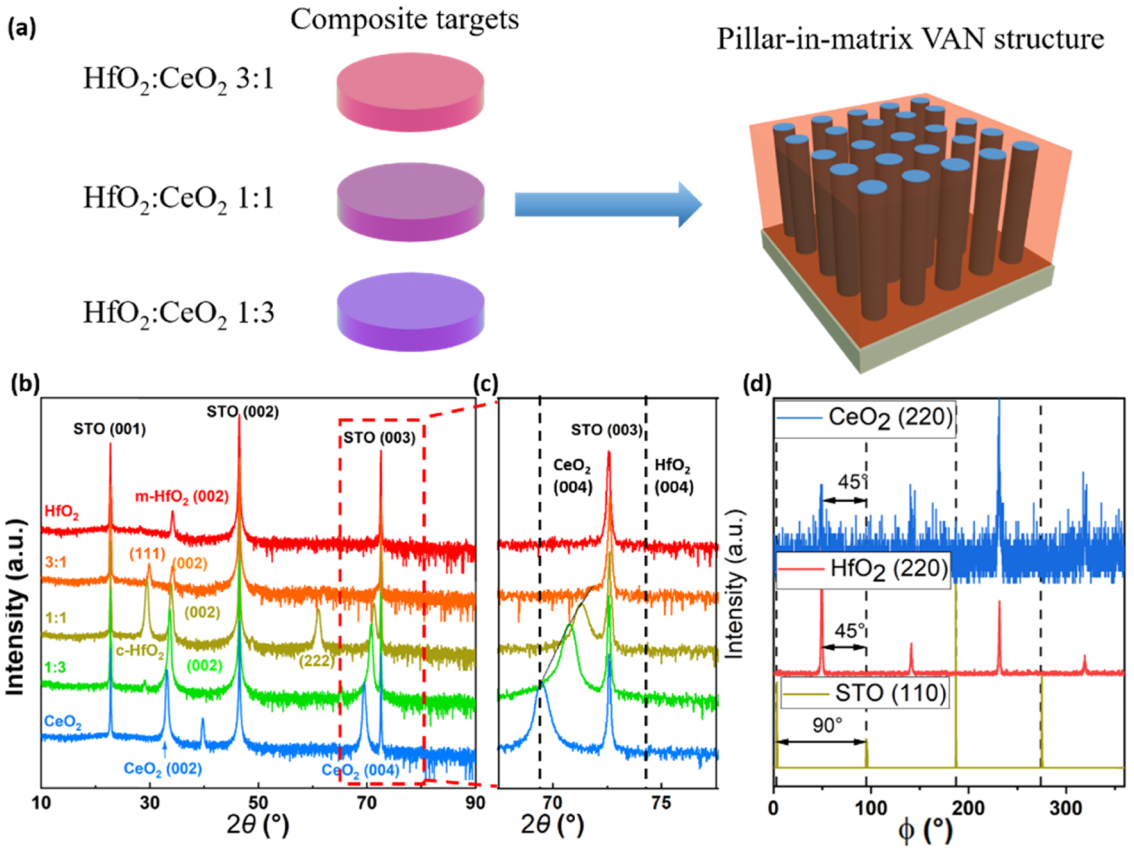

Figure 1. Schematics of the experimental design and XRD characterization of the deposited samples. (a) Schematics of the pillar-in-matrix VAN design with blue pillars and the red matrix corresponding to CeO_2 and HfO_2, respectively. (b) θ–2θ scans for all investigated films (HfO_2, HfO_2:CeO_2 = 3:1, 1:1, 1:3, and CeO_2). (c) Peak shifts of the CeO_2(004) from STO(003) with increasing CeO_2 concentration. (d) Φ-scan of the HfO_2:CeO_2 = 1:1 sample showing the 45° in-plane rotation of the HfO_2 and CeO_2 phases with respect to the STO substrate.

or pillar-in-matrix structures, giving rise to vertical boundaries with high density (lateral spacing of below 20 nm), have been shown to give rise to high-performance oxide-based memristors. It has been shown before that in epitaxial VAN systems containing two phases, one with enhanced ionic conductivity and one with electronic conduction along its vertical boundaries, high uniformity, high R_{HRS}/R_{LRS} ratios, and tunability can be achieved.[31−33] Previous studies have mostly focused on perovskite-based VAN systems for improved memristor applications, with very limited tunability demonstrated.

In this work, we have designed a HfO_2-based VAN system composed of HfO_2 and CeO_2 to achieve tailorable resistive switching properties with tunable density of the vertical-phase boundaries. By combining the two materials in a VAN structure, we expect to combine the merits from both materials (i.e., HfO_2 being a well-known dielectric and memristor material of significant industrial interest and CeO_2 being a mixed cation valence and ionic conducting system) as well as take advantage of the vertical-phase boundaries as the vertical oriented conducting filaments, and thus achieve a high-performance, forming-free memristor.

EXPERIMENTAL SECTION

HfO_2:CeO_2 targets with 3 different compositions (HfO_2:CeO_2 = 3:1, 1:1, 1:3), and pure HfO_2, CeO_2 targets, were prepared by conventional solid-state sintering, with the HfO_2 and CeO_2 powders mixed according to the stoichiometry of the composite prior to the sintering process. As shown in Figure 1a, the experimental design was to achieve the pillar-in-matrix VAN structure through the self-assembling process. The compositions of the targets were confirmed by energy-dispersive spectroscopy (EDS) to be HfO_2:CeO_2 = 3.06:1, 0.98:1, and 1:3.09. A pulsed laser deposition (PLD) technique was utilized to deposit all of the nanocomposite films onto STO(001) substrates. The deposition of all of the nanocomposite films was carried out in the same conditions, where the deposition temperature, oxygen partial pressure, laser frequency, laser energy density, number of laser shots, and substrate-target distance were maintained at 750 °C, 200 mTorr, 5 Hz, 5 J/cm^2, 3000, and 4.5 cm, respectively. After the deposition, all the films went through a cooling procedure with a cooling rate of 10 °C/min in a 200 Torr oxygen atmosphere to room temperature. For the samples used in electrical testing, a thin layer of $SrRuO_3$ (SRO) (~30 nm) was deposited as a bottom electrode prior to the nanocomposite films. The structural properties, including crystallinity and detailed microstructure, of the as-deposited samples were examined by X-ray diffraction (XRD, PANalytical Empyrean) and transmission electron microscopy (TEM, Thermo Scientific TALOS F200X), respectively. To evaluate the transport properties of the films, we fabricated top-contact electrodes Au (100 nm)/Ti (5 nm)/Pt (30 nm) by E-beam evaporation, where Pt is in contact with the oxide layer. Standard photolithography (lift-off) was used to form the circular contact pads with diameters of 50, 100, 150, 200, and 250 μm. The current−voltage (I–V) characteristics were measured using a Keithley 4200A-SCS Parameter Analyzer together with a Signatone Probe station. Ellipsometry was performed to characterize the optical property of the nanocomposite films using the RC2 spectroscopic ellipsometer (J.A. Woollam Company), and the real dielectric constants were extracted from the ellipsometry results. The fitting process was performed using the Spline or Gen-Osc models in the software from the aforementioned company (CompleteEase, J.A. Woollam Company).

https://doi.org/10.1021/acsaelm.1c00791
ACS Appl. Electron. Mater. 2021, 3, 5278−5286

RESULTS AND DISCUSSION

To obtain the structural information of the sample, XRD and TEM analyses were performed. Figure 1b shows the $\theta-2\theta$ scans of the investigated compositions, namely pure HfO_2, HfO_2:CeO_2 ratios of 3:1, 1:1, 1:3, and pure CeO_2. From the $\theta-2\theta$ scans, monoclinic HfO_2(002) is identified in the pure HfO_2 sample, while the cubic HfO_2(111) and (222), and the overlapping peaks (002) and (004) with CeO_2 in the Hf/Ce 1:1 ratio sample can be observed, indicating the phase separation in the HfO_2:CeO_2 1:1 sample. The (002) and (004) peaks suggest a nearly perfect match in the out-of-plane d-spacing of the HfO_2 and CeO_2 phases. In addition, the crystallinity of the HfO_2:CeO_2 1:1, 1:3, and pure CeO_2 films is shown to be better than that of HfO_2 and HfO_2:CeO_2 3:1 films due to the higher film peak intensity. Figure 1c demonstrates a clear peak shift of CeO_2(004) from 69.4 to 71.8°, showing evidence for strain coupling in the composite films.

The nominal out-of-plane strain $\varepsilon_\perp$ of HfO_2 and CeO_2(004) was then calculated from the reference lines marked on the plot: −3.6, −2.9, −1.5% for CeO_2(004) and 3.0, 3.9, 4.7% for HfO_2(004) in HfO_2:CeO_2 3:1, 1:1, and 1:3, respectively; the bulk lattice parameter is 5.15 Å for cubic HfO_2[34] and 5.41 Å for CeO_2.[35] The calculation reveals that CeO_2 experiences a compressive strain out-of-plane and thus a tensile strain in-plane, while HfO_2 has a tensile strain out-of-plane, suggesting an out-of-plane strain coupling between the two phases in VAN structures.[36] From the results, the out-of-plane strain of the HfO_2 and CeO_2 phases potentially helps stabilize the cubic phase HfO_2 at room temperature, rather than being the preferred monoclinic phase.[37] As shown in Figure S1, the TEM images and diffraction patterns of the pure HfO_2 sample indicate the presence of the monoclinic phase, agreeing with the results of the previous studies. The faceted pillar structure of the CeO_2 grown on STO substrate, and the epitaxial matching relation between the CeO_2 film and STO substrate, which is reflected by the diffraction patterns, are shown in Figure S2.

To further examine the in-plane matching relationships of the HfO_2:CeO_2 1:1 sample, ϕ-scans of STO(110), CeO_2(220), and HfO_2(220) were performed, and the results are shown in Figure 1d. The results indicate a 45° in-plane rotation of the film, agreeing with the previous investigation on CeO_2 growth on STO.[38] The HfO_2:CeO_2 composite system has been investigated in several studies.[39−42] While there is a low level of solubility of Hf in CeO_2 and Ce in HfO_2 as previously reported,[43,44] for simplicity here we label the phases as the dominant ones. The formation of HfO_2:CeO_2 solid solutions may also lead to the presence of cubic phase. Thus, compositional information of the samples is crucial for the understanding of the crystal structures and will be discussed in later sections.

TEM analysis was performed to directly investigate the microstructure and overall morphology of the as-deposited films. Figure 2a shows the TEM image of the HfO_2:CeO_2 1:1 sample, with a columnar structure with an average column width of ∼20 nm. The inset shows the schematic illustration of the ideal pillar-in-matrix VAN structure. Figure 2b presents the selected area electron diffraction (SAED) and shows a 45° in-plane rotation of the HfO_2:CeO_2 film to the STO substrate, which agrees with the results of ϕ-scan mentioned above. In the scanning transmission electron microscopy (STEM) image coupled with the energy-dispersive X-ray spectroscopy (EDX) mapping results in Figure 2c,d, columnar CeO_2 phase can be identified. Higher-magnification STEM images of the HfO_2:CeO_2 1:1 sample revealing the clear phase separation between HfO_2 and CeO_2 are shown in Figure S3. Figure 2a−d, together with Figure S3a,b presents collective evidence of the presence of VAN structure in the HfO_2:CeO_2 1:1 sample.

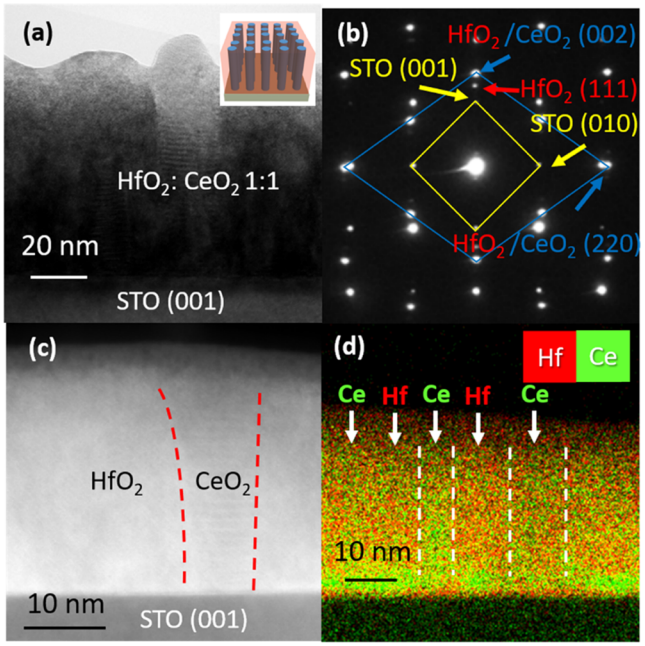

Figure 2. TEM images of the HfO_2:CeO_2 = 1:1 sample. (a) A columnar structure can be observed on the TEM image. The inset shows the schematic illustration of the pillar-in-matrix VAN structure. (b) Selected area electron diffraction (SAED) showing the rotation matching of the HfO_2:CeO_2 to STO substrate. (c) STEM image demonstrating the presence of columnar CeO_2 phase seggregation in the rather uniformly mixed film. (d) Energy-dispersive X-ray spectroscopy (EDX) showing Ce phase seggregation near the substarte interface and ceratin regions along the vertical direction.

The structural variation of the HfO_2:CeO_2 nanocomposites for all three compositions (HfO_2, HfO_2:CeO_2 1:1 and 1:3) is demonstrated in Figure 3. As shown in Figure 3a, the as-deposited pure HfO_2 demonstrates a columnar structure with textured growth and a vertical grain width of ∼15 nm, while the 1:3 sample consists of uniformly distributed pillars with a columnar width of ∼20 nm and resulting nanostructures in the film as shown in Figure 3c. The 1:1 sample shown in Figure 3b demonstrates uniform vertical phases with pillar diameters of ∼18 nm. Noticeably, the width of the vertical nanostructures increases with the concentration of CeO_2 within the film. The 1:1 sample presents the optimal VAN structure for memristor performance because it provides the most prominent phase separation compared to both 3:1 and 1:3 samples, where the phases of higher concentration dominate the overall growth process and form composite films with less obvious phase separation. To further demonstrate the phase separation, compositional analysis based on EDS mapping was performed in different regions in all three composite samples, as shown in Figures S6−S8 and Tables S1−S3. The HfO_2:CeO_2 3:1 and 1:3 samples show a relatively consistent composition throughout the sample areas, while the HfO_2:CeO_2 1:1 sample reveals composition variation across the sample areas. However, since the dimensions of the pillars are relatively small (∼10 nm) while the TEM foils are comparably thicker

https://doi.org/10.1021/acsaelm.1c00791
ACS Appl. Electron. Mater. 2021, 3, 5278−5286

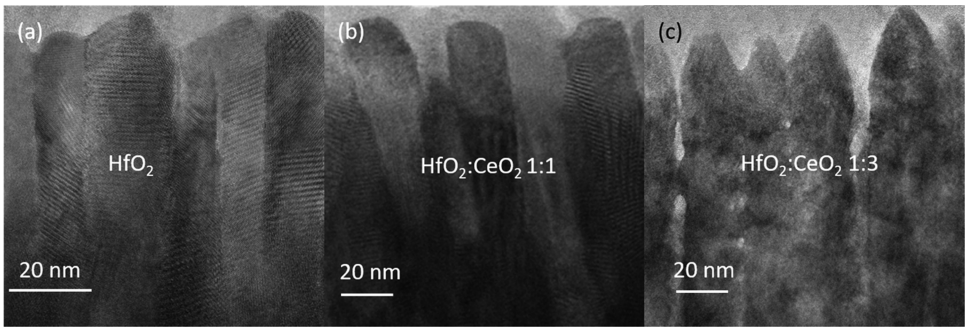

Figure 3. Structural evolution of HfO_2:CeO_2 composites with increasing CeO_2 concentration. (a) TEM image showing the columnar structure of the HfO_2 film. (b) TEM image indicating the VAN structure of the HfO_2:CeO_2 = 1:1 film. (c) TEM image showing the pyramid-like pillar growth in the HfO_2:CeO_2 = 1:3 film.

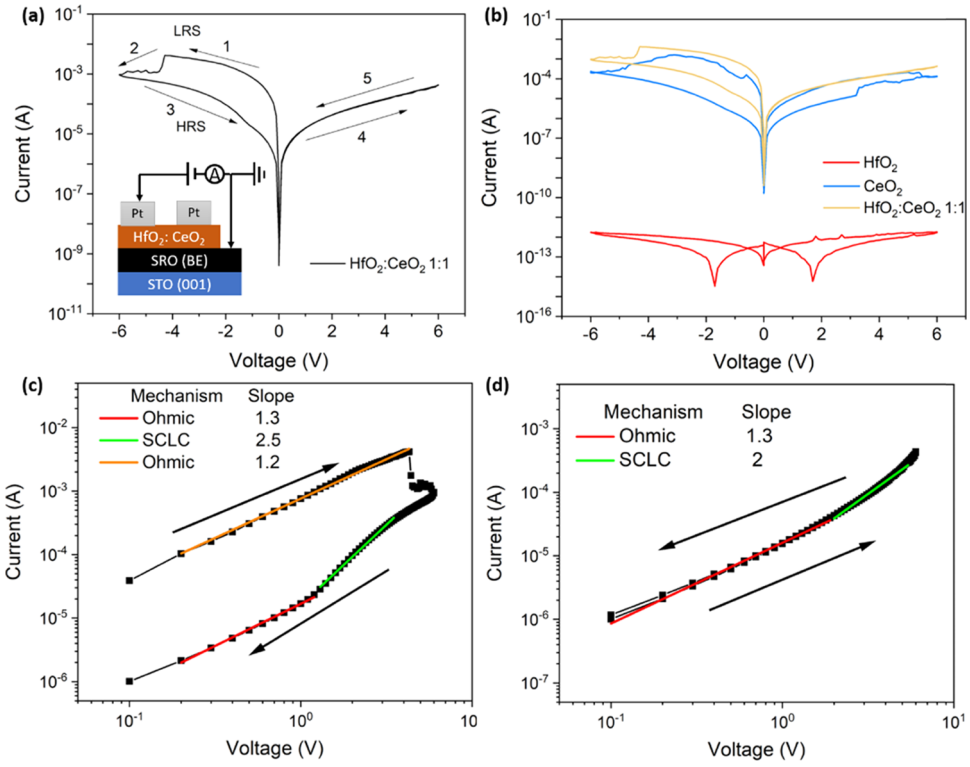

Figure 4. Electrical characterization and data fitting of the HfO_2:CeO_2 = 1:1 sample and two pure HfO_2 and CeO_2 samples. (a) I–V characteristics of HfO_2:CeO_2 1:1 showing resistive switching; a RESET process with R_{ON}/R_{OFF} ~ 10 is observed in the negative-voltage region (from LRS to HRS), while there is no switching in the positive-voltage region. The inset shows the device configuration; the film is sandwiched by Pt top electrodes and SRO bottom electrode on top of the STO substrate. (b) Comparison between HfO_2:CeO_2 1:1 and pure CeO_2, HfO_2. (c) I–V fitting of the RESET process in the negative-voltage region. (d) I–V fitting of the positive-voltage region.

(~20–30 nm), the overlapping of HfO_2 and CeO_2 pillars in the regions of interest in TEM and STEM images is highly possible, which could also cause the mixing of elements in EDX mapping and the ambiguity in phase separation. Combining the contrast in TEM and STEM images and the composition variation in EDX mapping as well as the peaks indicating the presence of c-HfO_2 and CeO_2, it is clear that the 1:1 sample demonstrates obvious HfO_2 and CeO_2 phase separation. To correlate the microstructure with the device performance, XRD analysis of the films deposited on SRO bottom electrodes was also performed, as shown in Figure S9.

To gain a deeper understanding of the crystal structures of the films, and the underlying mechanisms for the lattice variation, especially HfO_2:CeO_2 3:1 and 1:3, the compositions of the composite samples were extracted based on EDS mappings. According to Table S4, Figures S5 and S10, the HfO_2:CeO_2 1:3 sample was believed to be mostly in cubic phase due to phase mixing,[39] while the monoclinic phase HfO_2 was expected to be dominant in HfO_2:CeO_2 3:1. As the highest solubility limit of HfO_2 in CeO_2 was reported to be x = 0.5,[39,41,45] the phase variation thus originates from the change in composition. In HfO_2:CeO_2 3:1, the excess HfO_2 could return to monoclinic phase, which is more stable at room temperature. The phase variation is shown in Figure S10 as the structural evolution. It is clearly demonstrated that pure HfO_2 and HfO_2:CeO_2 3:1 samples have a similar structure, while HfO_2:CeO_2 1:3 has a similar structure to that of CeO_2, supporting the aforementioned discussion. A clear trend in the grain morphology transition, shown in Figure S11, is from columnar grains with minor tilting (in both HfO_2 and

https://doi.org/10.1021/acsaelm.1c00791
ACS Appl. Electron. Mater. 2021, 3, 5278–5286

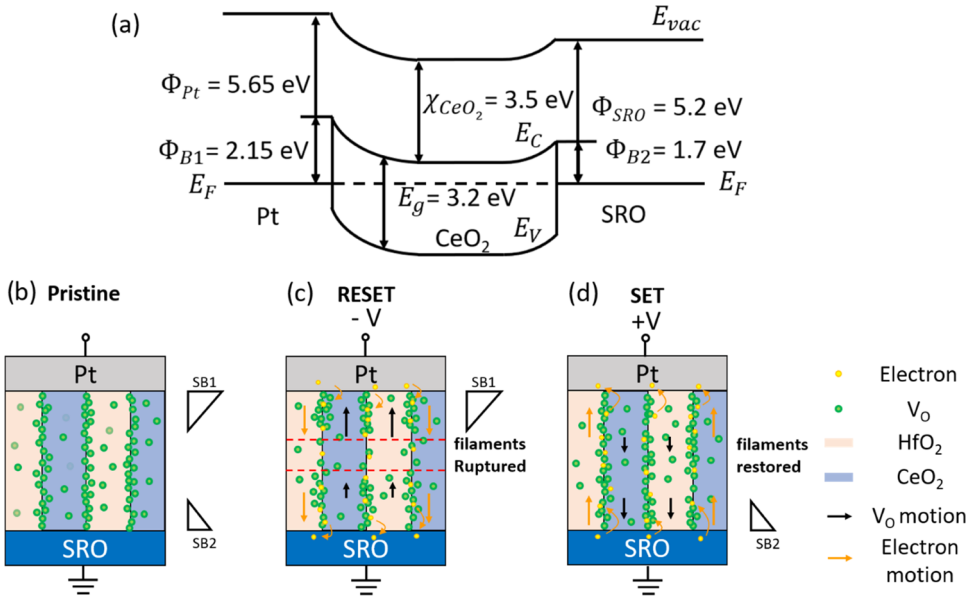

Figure 5. Schematics of the energy band diagram of the Pt/HfO_2:CeO_2 1:1/SRO structure and filament rupture and formation processes. (a) Energy band diagram showing Schottky barriers at both Pt/CeO_2 and CeO_2/SRO interfaces. (b) Pristine state of the HfO_2:CeO_2 1:1 device. Conduction filaments locate at the phase boundaries. (c) In the RESET process, positively charged oxygen vacancies move toward the Pt top electrode. The higher electric field near the Pt/HfO_2:CeO_2 1:1 interface (Schottky barrier 1) results in more oxygen vacancy movement, leading to the rupture of conducting filaments. (d) In the SET process, the oxygen vacancies move toward the $SrRuO_3$ bottom electrode, restoring the conducting filaments.

HfO_2:CeO_2 3:1, Figure S10a,b) to better-aligned columnar gains (in HfO_2:CeO_2 1:1, Figure S10c) to, finally, the faceted pillar-like grains (in the cases of HfO_2:CeO_2 1:3 and CeO_2, Figure S10d,e). Such grain morphology tuning can be well explained by the 50% solubility limit in the HfO_2:CeO_2 system. This observed structural evolution, shown in Figure S10, hereby demonstrates a simple and effective way of tuning the vertical structure as well as the density of the vertical grain and phase boundaries. The properties of each composition are summarized and shown in Table S5.

With the desirable VAN structure achieved in the HfO_2:CeO_2 1:1 sample, the electrical measurements of all fabricated devices are followed to compare the resistive switching properties among all compositions. Among all samples, the HfO_2:CeO_2 1:1 sample demonstrates several salient characteristics: (1) electroforming-free resistive switching; (2) asymmetrical switching behavior; and (3) the lowest resistivity (1.98×10^2 Ω·m) among all the investigated compositions. Furthermore, the above-mentioned characteristics reveal the potential of the VAN HfO_2:CeO_2 1:1 for memristor applications.

The $I-V$ characteristic of HfO_2:CeO_2 1:1 is presented in Figure 4a with the device configuration shown in the inset. The HfO_2:CeO_2 1:1 film is sandwiched by Pt top electrodes and SRO bottom electrodes on a STO(001) substrate. As shown in Figure 4a, the device using HfO_2:CeO_2 1:1 as the dielectric layer shows clearly the resistive switching behavior or the hysteresis loop of the current versus voltage ($I-V$) characteristic. The ratio between the high-resistance state (R_{HRS}) and the low-resistance state (R_{LRS}) is around 10 under the negative bias of −1 V. However, there is negligible $I-V$ hysteresis at positive voltage bias. This asymmetrical $I-V$ response of the sample is possibly caused by the transition from ionic switching, namely the rupture of the conducting filament via oxygen vacancy migration, as illustrated later in Figure 5, to electronic switching, which is the charge trapping and de-trapping, due to the asymmetric Schottky barrier height of the Pt/HfO_2:CeO_2 1:1/SRO structure.[7] The comparison between HfO_2:CeO_2 1:1 and pure HfO_2 and CeO_2 is shown in Figure 4b; the sizes of the Au/Ti/Pt electrodes for HfO_2:CeO_2 1:1, HfO_2, and CeO_2 devices are 200, 200, and 150 μm, respectively. The plot shows an interesting behavior of the films: HfO_2 is highly insulating with a resistivity $\rho \sim 10^{12}$ Ω·m, and shows capacitive $I-V$ characteristics. On the other hand, the pure CeO_2 and nanocomposite HfO_2:CeO_2 = 1:1 are more conductive, with resistivities ranging from $\rho \sim 10^2$ to 10^4 Ω·m. More importantly, resistive switching behavior is observed in both CeO_2 and HfO_2:CeO_2 1:1 with ON/OFF ratios ranging from 10 to 10^2, with no indication of the electroforming process reported in a previous work.[46] The electroforming-free nature of the mentioned samples indicates the presence of conductive paths in the as-deposited films prior to the actual $I-V$ measurements. The asymmetry of the $I-V$ loop then corresponds to the movement of V_o back and forth towards the Pt electrode. The behavior is similar to the VAN systems demonstrated previously,[30,33] but significantly now in a composite binary system, which has a much greater industrial potential. The other samples, with less obvious VAN structure between the CeO_2 and HfO_2 phases, as shown in Supporting Information Figures S4 and S5, consist of less conductive channels and thus demonstrate no forming-free switching behavior.

Another aforementioned characteristic of the HfO_2:CeO_2 1:1 is low resistivity, as observed in the LRS from HfO_2:CeO_2 1:1 ($\rho = 1.98 \times 10^2$ Ω·m) to CeO_2 ($\rho = 2.28 \times 10^2$ Ω·m), considering the fact that the HfO_2:CeO_2 1:1 sample consists of ~50% insulating HfO_2. This phenomenon is not observed in the other two samples of HfO_2:CeO_2 3:1 and 1:3, where both of the samples demonstrate insulating nature with resistivity $\rho \sim 10^9$ Ω·m; data of the $I-V$ characteristics is shown in

https://doi.org/10.1021/acsaelm.1c00791
ACS Appl. Electron. Mater. 2021, 3, 5278−5286

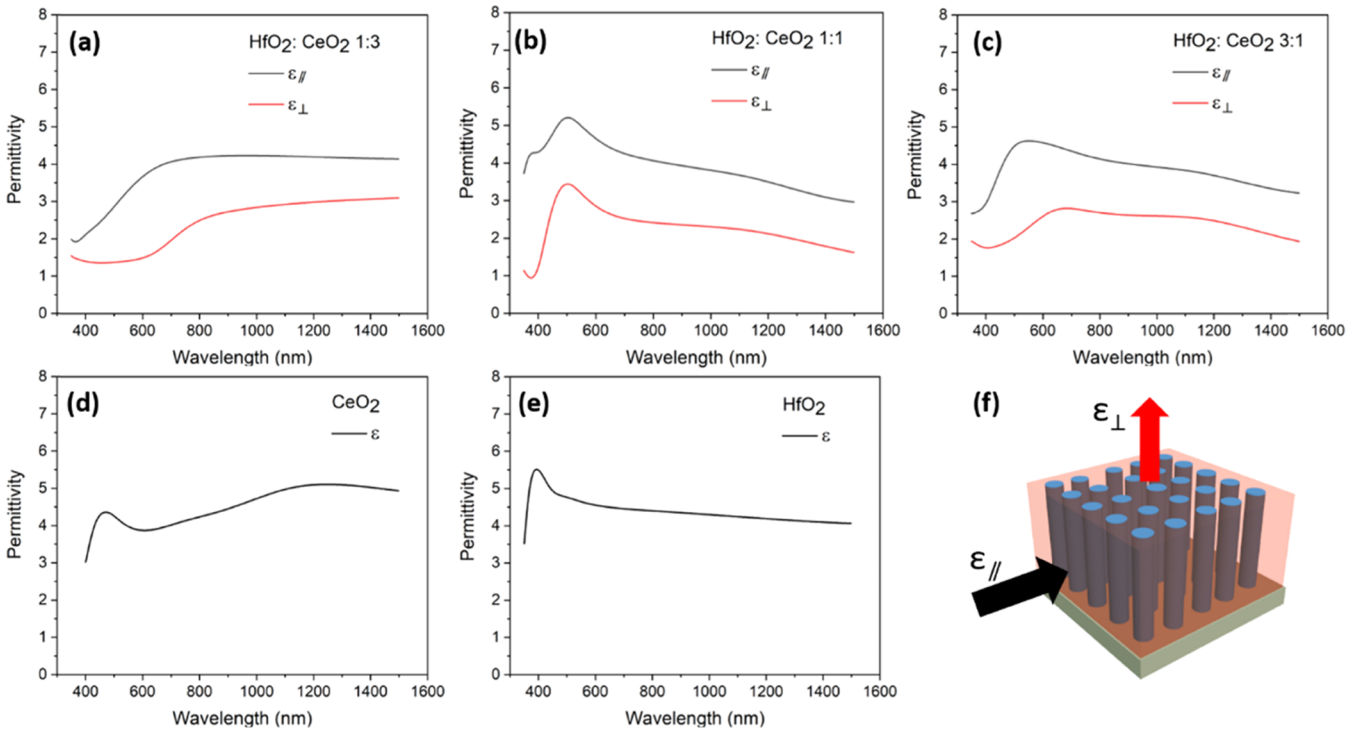

Figure 6. Dielectric permittivity data derived by ellipsometry and the fitting process. The relative permittivity of (a) HfO_2:CeO_2 1:3, (b) HfO_2:CeO_2 1:1, (c) HfO_2:CeO_2 3:1, (d) CeO_2, and (e) HfO_2. (f) Illustration of the sample geometry and ellipsometry configuration; the in-plane and out-of-plane directions are indicated as black and red arrows, respectively.

Supporting Information Figure S12. A reasonable level of conductance is necessary to eliminate the high-voltage-forming process of very-high-resistance films.

As discussed above, the HfO_2:CeO_2 1:1 sample demonstrates several merits for RRAM applications. The electroforming-free behavior is much preferred in the RRAM application since it avoids the initial electroforming process of conductive filaments in the switching layer, which results in non-uniformity and additional energy consumption.[47] Hence, the burdensome electroforming procedures and their challenging realization in the circuit level also bring challenges to the development of RRAM. Also, the asymmetrical $I-V$ characteristic of the HfO_2:CeO_2 1:1 sample can be a potential solution to the sneak current problem, which causes reading errors and unnecessary energy consumption in the crossbar arrays.[48]

With the merits of the HfO_2:CeO_2 1:1 sample discussed, the switching mechanism is worth a detailed discussion. The log−log plots of the $I-V$ characteristics of both devices (HfO_2:CeO_2 1:1 and CeO_2) were plotted (shown in Figures 4c,d and S13) to elucidate the conduction mechanism, which involves the formation of conducting paths of oxygen vacancies in LRS; also, the space charge limited conduction (SCLC) in HRS, whereby the conduction paths are ruptured, is proposed as the dominant conduction mechanism.[21,46] The higher conductivity observed in the 1:1 sample is related to its structural features: the VAN structure, where the higher density of phase boundaries separating CeO_2 and the HfO_2 provides conducting channels and thus improves the conductivity of the tested device.[29,32]

It is known that the typical $I-V$ characteristic of resistive switching materials can follow a power-law behavior, $J \propto V^m$, where $m = 1$ signifies ohmic behavior, and $m = 2$ represents trap-free SCLC, while $m > 2$ implies SCLC accompanied by trap filling.[49] In the HfO_2:CeO_2 1:1 sample shown in Figure 4c, the device showed ohmic conduction in the negative bias regime with a slope of 1.2 in the LRS before switching to the HRS. The reverse sweep $I-V$ showed a trap-free SCLC conduction at higher bias, and ohmic conduction as the bias was lowered. But, in the positive bias regime, there was very little hysteresis (ON/OFF ∼ 1.06) observed between the forward and reverse sweep, as shown in Figure 4d, indicating an asymmetrical switching behavior of the $I-V$ characteristics. This asymmetry of the $I-V$ characteristic might arise from the asymmetric Pt/HfO_2:CeO_2 1:1/SRO structure.[48,50] To illustrate the electronic structure of the Pt/HfO_2:CeO_2 1:1/SRO device, a schematic of the energy band diagram is shown in Figure 5a. According to previous literature, the work function of $SrRuO_3$ (SRO) is 5.2 eV,[51] the work function of Pt is about 5.65 eV,[52] and the electron affinity and band gap of CeO_2 are 3.5 and 3.2 eV,[53] respectively. Considering that there are no references of either the computational or experimental data of the band gap and electron affinity at grain boundaries for the HfO_2:CeO_2 system, and that the conduction is enhanced in the composite films, the lower values of CeO_2 are therefore used for the illustrative band diagram drawing in Figure 5, rather than the values of HfO_2 (band gap ∼ 5.8 eV and electron affinity ∼ 2.0 eV[54]). Assuming no Fermi level pinning at the metal/oxide interfaces and the CeO_2 is slightly n-type doped due to the presence of oxygen vacancies, the Schottky barriers at the two interfaces, according to the equation $\Phi_B = \Phi_m - \chi$, where Φ_B is the Schottky barrier height, Φ_m is the work function of the top/bottom electrode, and χ is the electron affinity of the insulating film in-between the electrodes, are then shown to be around 2.15 and 1.7 eV, respectively, resulting in an asymmetric back-to-back Schottky barrier contact. As discussed previously, the switching behavior in the negative-voltage region is dominated by the rupture of the already present conduction paths in the film, and is considered

https://doi.org/10.1021/acsaelm.1c00791
ACS Appl. Electron. Mater. 2021, 3, 5278−5286

to be ionic switching. On the other hand, in the positive-voltage region, the conduction mechanism demonstrates complete SCLC and the switching is realized by charge trapping and de-trapping, which is considered as electronic switching. Figure 5b–d demonstrates the schematics of the possible switching processes. During the RESET process, the higher Schottky barrier at the Pt/HfO_2:CeO_2 1:1 interface makes it difficult to inject electrons into the switching layer. As a result, the higher electric field at the Schottky barrier causes field-induced oxygen vacancy migration that results in the further rupture of conduction paths, as shown in Figure 5c. During the SET process, electron injection into the switching layer is more facile due to the lower Schottky barrier at the HfO_2:CeO_2 1:1/SRO interface. Consequently, the lower electric field at the Schottky barrier is less sufficient to move the oxygen vacancies and the less mobile oxygen vacancies serve as electronic traps; the electronic trapping and de-trapping becomes the prevailing mechanism.[50] The partially restored conduction paths, indicated by the SCLC in the SET process, are schematically shown in Figure 5d as the positively charged oxygen vacancies gradually move toward the bottom electrode.

In the CeO_2 sample, the fitting results are shown in Figure S13. The device showed filamentary switching in the negative-voltage region, while SCLC is shown to be responsible for the LRS in the positive-voltage region. The conduction mechanism of our samples was seen to be consistent with previously reported results for CeO_2.[21,30]

To elucidate the anisotropic nature of the VAN structures, the optical dielectric response was measured by an ellipsometer and the relative permittivity was fitted from the ellipsometry results using an isotropic model for HfO_2 and CeO_2 films and an anisotropic model for the nanocomposite ones. From Figure 6a–c, the anisotropy in the permittivity, i.e., out-of-plane (OP) permittivity $\varepsilon_\perp$ being lower than in-plane (IP) permittivity $\varepsilon_\parallel$, is revealed. Figure 6f illustrates the directions of the measured IP and OP permittivity, $\varepsilon_\parallel$ and $\varepsilon_\perp$. The pure HfO_2 and CeO_2, however, shows an isotropic relative permittivity of 3–5 throughout the tested wavelength region, as shown in Figure 6d,e. This intriguing phenomenon might be explained by the vertical structures observed in the HfO_2:CeO_2 3:1, 1:1, and 1:3 samples, where the vertical grain boundaries and phase boundaries are taken as effective conduction paths for electrons and charged ions.[55] Alternative fitting of the HfO_2:CeO_2 3:1 and 1:3 films using an isotropic model is also performed. The error in fitting of the HfO_2:CeO_2 1:1 film with an isotropic model is much larger than that when the anisotropic model is used, indicating the anisotropic nature in the dielectric response. The other two samples of 3:1 and 1:3 show comparable errors, with the isotropic model suggesting less obvious anisotropy in these two samples, due to the less prominent vertical-phase boundaries compared to that of the 1:1 case. The fitting results are attached in Supporting Information as Figure S14.

As the first attempt to explore the properties of HfO_2:CeO_2 VAN systems for memristor applications, the current devices show great tunability in the electrical properties and potential in the integration of multiple functions for memory and optoelectronic applications. Such a system, with its effectiveness demonstrated, provides insight into the fundamental switching mechanism and further broadens the avenue of defect engineering in memristors. Although with great potential in the memristor application, the current devices have clear drawbacks, which are reflected in the missing of ideal endurance and retention data. Looking to the future, the HfO_2:CeO_2 VAN system could be further improved. From the structure point of view, the existing VAN structure in the HfO_2:CeO_2 1:1 film could give further improved scaling with finer phase separation, which can be tuned by altering the growth kinetics. The operating voltage (~6 V), device endurance, and retention properties of the HfO_2:CeO_2 1:1 film could be improved by reducing the film thickness as well as optimizing the growth conditions, including the growth rate, oxygen partial pressure, and temperature. Potential directions for exploration on stable endurance and retention properties lie in stabilizing the HfO_2:CeO_2 phase boundaries for oxygen vacancy drift and diffusion. To further elucidate the conduction mechanism of the proposed HfO_2:CeO_2 1:1 device, time-dependent as well as temperature-dependent I–V measurements should be attempted.

CONCLUSIONS

In this paper, we have demonstrated HfO_2:CeO_2 vertically aligned nanocomposites (VANs) with HfO_2 and CeO_2 molar ratio of 1:1 on $SrTiO_3$(001) substrates using pulsed laser deposition. The tunability of the arrangement of the vertical grains/phases and the resulting grain/phase boundary density has also been demonstrated by TEM and STEM. The VAN films enable electroforming-free resistive switching in the HfO_2:CeO_2 1:1 composition film, where conductivity is enhanced compared to the single-phase counterparts. Enhanced anisotropic dielectric responses were observed in the HfO_2:CeO_2 1:1 film compared to the pure HfO_2 and CeO_2 films, consistent with the hypothesis that vertical boundaries provide easy paths for electron and ion transport. The electroforming-free resistive switching and enhanced conductivity in the HfO_2:CeO_2 1:1 film provide evidence for an effective way of manipulating the accumulation of the oxygen vacancies in a simple binary composite system of industrial potential, while the anisotropic dielectric responses demonstrate potential in anisotropic optical designs.

ASSOCIATED CONTENT

Supporting Information

The Supporting Information is available free of charge at https://pubs.acs.org/doi/10.1021/acsaelm.1c00791.

Structural characterization (XRD, TEM, STEM & EDX mapping); electrical characterization (I–V plot and fitting); optical characterization (permittivity); all as function of compositions (PDF)

AUTHOR INFORMATION

Corresponding Author

Haiyan Wang − *School of Materials Engineering, Purdue University, West Lafayette, Indiana 47907, United States; School of Electrical and Computer Engineering, Purdue University, West Lafayette, Indiana 47907, United States;* orcid.org/0000-0002-7397-1209; Email: hwang00@purdue.edu

Authors

Hongyi Dou − *School of Materials Engineering, Purdue University, West Lafayette, Indiana 47907, United States*

Xingyao Gao − *School of Materials Engineering, Purdue University, West Lafayette, Indiana 47907, United States*

https://doi.org/10.1021/acsaelm.1c00791
ACS Appl. Electron. Mater. 2021, 3, 5278–5286

Di Zhang − *School of Materials Engineering, Purdue University, West Lafayette, Indiana 47907, United States*
Samyak Dhole − *Department of Materials Design and Innovation, University at Buffalo, the State University of New York, Buffalo, New York 14260, United States*
Zhimin Qi − *School of Materials Engineering, Purdue University, West Lafayette, Indiana 47907, United States*
Bo Yang − *School of Materials Engineering, Purdue University, West Lafayette, Indiana 47907, United States*
Md Nazmul Hasan − *Department of Materials Design and Innovation, University at Buffalo, the State University of New York, Buffalo, New York 14260, United States*
Jung-Hun Seo − *Department of Materials Design and Innovation, University at Buffalo, the State University of New York, Buffalo, New York 14260, United States;* orcid.org/0000-0002-5039-2503
Quanxi Jia − *Department of Materials Design and Innovation, University at Buffalo, the State University of New York, Buffalo, New York 14260, United States*
Markus Hellenbrand − *Department of Materials Science and Metallurgy, University of Cambridge, Cambridge CB3 0FS, U.K.;* orcid.org/0000-0002-5811-5228
Judith L. MacManus-Driscoll − *Department of Materials Science and Metallurgy, University of Cambridge, Cambridge CB3 0FS, U.K.;* orcid.org/0000-0003-4987-6620
Xinghang Zhang − *School of Materials Engineering, Purdue University, West Lafayette, Indiana 47907, United States;* orcid.org/0000-0002-8380-8667

Complete contact information is available at: https://pubs.acs.org/10.1021/acsaelm.1c00791

Notes

The authors declare no competing financial interest.

■ ACKNOWLEDGMENTS

The US-UK collaborative effort was funded by the U.S. National Science Foundation (ECCS-1902644 (Purdue University), ECCS-1902623 (University at Buffalo, SUNY)) and the EPRSC grant EP/T012218/1. The Cambridge investigators further acknowledge funding from the Royal Academy of Engineering—CIET1819_24, the Leverhulme Trust grant RPG-2015-017, and EPSRC grants EP/N004272/1 and EP/P007767/1.

■ REFERENCES

(1) Xu, X.; Lv, H.; Liu, H.; Gong, T.; Wang, G.; Zhang, M.; Li, Y.; Liu, Q.; Long, S.; Liu, M. Superior Retention of Low-Resistance State in Conductive Bridge Random Access Memory with Single Filament Formation. *IEEE Electron Device Lett.* **2015**, *36*, 129−131.
(2) Zhuang, W. W.; Pan, W.; Ulrich, B. D.; Lee, J. J.; Stecker, L.; Burmaster, A.; Evans, D. R.; Hsu, S. T.; Tajiri, M.; Shimaoka, A.; Inoue, K.; Naka, T.; Awaya, N.; Sakiyama, K.; Wang, Y.; Liu, S. Q.; Wu, N. J.; Ignatiev, A. In *Novell Colossal Magnetoresistive Thin Film Nonvolatile Resistance Random Access Memory (RRAM)*, Technical Digest—International Electron Devices Meeting, 2002; pp 193−196.
(3) Lee, S.; Lee, J. S.; Park, J.-B.; Koo Kyoung, Y.; Lee, M.-J.; Won Noh, T. Anomalous Effect Due to Oxygen Vacancy Accumulation below the Electrode in Bipolar Resistance Switching Pt/Nb:$SrTiO_3$ Cells. *APL Mater.* **2014**, *2*, No. 066103.
(4) Wang, P.; Yi, W.; Chen, J.; Ito, S.; Cui, C.; Sekiguchi, T. Oxygen Vacancy Migration along Dislocations in SrTiO3 Studied by Cathodoluminescence. *J. Phys. D: Appl. Phys.* **2019**, *52*, No. 475103.
(5) Szot, K.; Speier, W.; Bihlmayer, G.; Waser, R. Switching the Electrical Resistance of Individual Dislocations in Single-Crystalline $SrTiO_3$. *Nat. Mater.* **2006**, *5*, 312−320.
(6) Ha, S. D.; Ramanathan, S. Adaptive Oxide Electronics: A Review. *J. Appl. Phys.* **2011**, *110*, No. 071101.
(7) Tao, D. W.; Chen, J. B.; Jiang, Z. J.; Qi, B. J.; Zhang, K.; Wang, C. W. Making Reversible Transformation from Electronic to Ionic Resistive Switching Possible by Applied Electric Field in an Asymmetrical Al/TiO_2/FTO Nanostructure. *Appl. Surf. Sci.* **2020**, *502*, No. 144124.
(8) Gale, E. TiO2 -Based Memristors and ReRAM: Materials, Mechanisms and Models (a Review). *Semicond. Sci. Technol.* **2014**, *29*, No. 104004.
(9) Jeong, D. S.; Schroeder, H.; Breuer, U.; Waser, R. Characteristic Electroforming Behavior in Pt/TiO_2/Pt Resistive Switching Cells Depending on Atmosphere. *J. Appl. Phys.* **2008**, *104*, No. 123716.
(10) Kwon, D. H.; Kim, K. M.; Jang, J. H.; Jeon, J. M.; Lee, M. H.; Kim, G. H.; Li, X. S.; Park, G. S.; Lee, B.; Han, S.; Kim, M.; Hwang, C. S. Atomic Structure of Conducting Nanofilaments in TiO_2 Resistive Switching Memory. *Nat. Nanotechnol.* **2010**, *5*, 148−153.
(11) Sedghi, N.; Li, H.; Brunell, I. F.; Dawson, K.; Guo, Y.; Potter, R. J.; Gibbon, J. T.; Dhanak, V. R.; Zhang, W. D.; Zhang, J. F.; Hall, S.; Robertson, J.; Chalker, P. R. Enhanced Switching Stability in Ta_2O_5 Resistive RAM by Fluorine Doping. *Appl. Phys. Lett.* **2017**, *111*, No. 092904.
(12) Macaluso, R.; Mosca, M.; Costanza, V.; D'Angelo, A.; Lullo, G.; Caruso, F.; Calì, C.; Di Franco, F.; Santamaria, M.; Di Quarto, F. Resistive Switching Behaviour in ZnO and VO_2 Memristors Grown by Pulsed Laser Deposition. *Electron. Lett.* **2014**, *50*, 262−263.
(13) Song, M.; Lee, H.; Seo, D. H.; Lee, H. J.; Kim, J. S.; Cho, H. S.; Lyu, H. K.; Seo, S.; Lee, M. J. Improved Distribution of Resistance Switching through Localized Ti-Doped NiO Layer with $InZnO_x$/CuO_x Oxide Diode. *IEEE J. Electron Devices Soc.* **2018**, *6*, 905−909.
(14) Russo, U.; Ielmini, D.; Cagli, C.; Lacaita, A. L. Filament Conduction and Reset Mechanism in NiO-Based Resistive-Switching Memory (RRAM) Devices. *IEEE Trans. Electron Devices* **2009**, *56*, 186−192.
(15) Lin, K.-L.; Hou, T.-H.; Shieh, J.; Lin, J.-H.; Chou, C.-T.; Lee, Y.-J. Electrode Dependence of Filament Formation in HfO_2 Resistive-Switching Memory. *J. Appl. Phys.* **2011**, *109*, No. 084104.
(16) Murdoch, B. J.; McCulloch, D. G.; Ganesan, R.; McKenzie, D. R.; Bilek, M. M. M.; Partridge, J. G. Memristor and Selector Devices Fabricated from $HfO_{2-X}N_x$. *Appl. Phys. Lett.* **2016**, *108*, No. 143504.
(17) Brivio, S.; Frascaroli, J.; Spiga, S. Role of Metal-Oxide Interfaces in the Multiple Resistance Switching Regimes of Pt/HfO2/TiN Devices. *Appl. Phys. Lett.* **2015**, *107*, No. 023504.
(18) Long, B. M.; Mandal, S.; Livecchi, J.; Jha, R. Effects of Mg-Doping on HfO_2-Based ReRAM Device Switching Characteristics. *IEEE Electron Device Lett.* **2013**, *34*, 1247−1249.
(19) Dirkmann, S.; Kaiser, J.; Wenger, C.; Mussenbrock, T. Filament Growth and Resistive Switching in Hafnium Oxide Memristive Devices. *ACS Appl. Mater. Interfaces* **2018**, *10*, 14857−14868.
(20) Younis, A.; Chu, D.; Mihail, I.; Li, S. Interface-Engineered Resistive Switching: CeO_2 Nanocubes as High-Performance Memory Cells. *ACS Appl. Mater. Interfaces* **2013**, *5*, 9429−9434.
(21) Zhang, J.; Zhao, H.; Wei, F.; Yang, M.; Yang, Z.; Chen, Q.; Chen, J. Resistive Switching Behaviour of Highly Epitaxial CeO2 Thin Film for Memory Application. *Phys. Status Solidi RRL* **2014**, *8*, 95−99.
(22) Jabeen, S.; Ismail, M.; Rana, A. M.; Ahmed, E. Impact of Work Function on the Resistive Switching Characteristics of M/ZnO/CeO_2/Pt Devices. *Mater. Res. Express* **2017**, *4*, No. 056401.
(23) Lin, C. Y.; Lee, D. Y.; Wang, S. Y.; Lin, C. C.; Tseng, T. Y. Reproducible Resistive Switching Behavior in Sputtered CeO_2 Polycrystalline Films. *Surf. Coat. Technol.* **2008**, *203*, 480−483.
(24) Ortega-Hernandez, R.; Coll, M.; Gonzalez-Rosillo, J.; Palau, A.; Obradors, X.; Miranda, E.; Puig, T.; Suñe, J. Resistive Switching in CeO_2/$La_{0.8}Sr_{0.2}MnO_3$ Bilayer for Non-Volatile Memory Applications. *Microelectron. Eng.* **2015**, *147*, 37−40.

(25) Ismail, M.; Nisa, S.-U.; Rana, A. M.; Akbar, T.; Lee, J.; Kim, S. Enhancement of Resistive Switching Performance by Introducing a Thin Non-Stoichiometric CeO_{2-x} Switching Layer in TiO_2-Based Resistive Random Access Memory. *Appl. Phys. Lett.* **2019**, *114*, No. 012101.
(26) Nail, C.; Molas, G.; Blaise, P.; Piccolboni, G.; Sklenard, B.; Cagli, C.; Bernard, M.; Roule, A.; Azzaz, M.; Vianello, E.; Carabasse, C.; Berthier, R.; Cooper, D.; Pelissier, C.; Magis, T.; Ghibaudo, G.; Vallee, C.; Bedeau, D.; Mosendz, O.; De Salvo, B.; Perniola, L. In *Understanding RRAM Endurance, Retention and Window Margin Trade-off Using Experimental Results and Simulations*, 2016 IEEE International Electron Devices Meeting (IEDM); IEEE, 2017; pp 4.5.1−4.5.4.
(27) Esch, F.; Fabris, S.; Zhou, L.; Montini, T.; Africh, C.; Fornasiero, P.; Comelli, G.; Rosei, R. Chemistry: Electron Localization Determines Defect Formation on Ceria Substrates. *Science* **2005**, *309*, 752−755.
(28) Mogensen, M.; Sammes, N. M.; Tompsett, G. A. Physical, Chemical and Electrochemical Properties of Pure and Doped Ceria. *Solid State Ionics* **2000**, *129*, 63−94.
(29) Lanza, M.; Zhang, K.; Porti, M.; Nafría, M.; Shen, Z. Y.; Liu, L. F.; Kang, J. F.; Gilmer, D.; Bersuker, G. Grain Boundaries as Preferential Sites for Resistive Switching in the HfO_2 Resistive Random Access Memory Structures. *Appl. Phys. Lett.* **2012**, *100*, No. 123508.
(30) Cho, S.; Yun, C.; Tappertzhofen, S.; Kursumovic, A.; Lee, S.; Lu, P.; Jia, Q.; Fan, M.; Jian, J.; Wang, H.; Hofmann, S.; MacManus-Driscoll, J. L. Self-Assembled Oxide Films with Tailored Nanoscale Ionic and Electronic Channels for Controlled Resistive Switching. *Nat. Commun.* **2016**, *7*, No. 12373.
(31) Su, Q.; Yoon, D.; Chen, A.; Khatkhatay, F.; Manthiram, A.; Wang, H. Vertically Aligned Nanocomposite Electrolytes with Superior Out-of-Plane Ionic Conductivity for Solid Oxide Fuel Cells. *J. Power Sources* **2013**, *242*, 455−463.
(32) Yang, S. M.; Lee, S.; Jian, J.; Zhang, W.; Lu, P.; Jia, Q.; Wang, H.; Won Noh, T.; Kalinin, S. V.; MacManus-Driscoll, J. L. Strongly Enhanced Oxygen Ion Transport through Samarium-Doped CeO_2 Nanopillars in Nanocomposite Films. *Nat. Commun.* **2015**, *6*, No. 8588.
(33) Lee, S.; Sangle, A.; Lu, P.; Chen, A.; Zhang, W.; Lee, J. S.; Wang, H.; Jia, Q.; MacManus-Driscoll, J. L. Novel Electroforming-Free Nanoscaffold Memristor with Very High Uniformity, Tunability, and Density. *Adv. Mater.* **2014**, *26*, 6284−6289.
(34) Zhao, X.; Vanderbilt, D. First-Principles Study of Structural, Vibrational, and Lattice Dielectric Properties of Hafnium Oxide. *Phys. Rev. B* **2002**, *65*, No. 233106.
(35) Babitha, K. K.; Sreedevi, A.; Priyanka, K. P.; Sabu, B.; Varghese, T. Structural Characterization and Optical Studies of CeO2 Nanoparticles Synthesized by Chemical Precipitation. *Indian J. Pure Appl. Phys.* **2015**, *53*, 596−603.
(36) Chen, A.; Bi, Z.; Jia, Q.; Macmanus-Driscoll, J. L.; Wang, H. Microstructure, Vertical Strain Control and Tunable Functionalities in Self-Assembled, Vertically Aligned Nanocomposite Thin Films. *Acta Mater.* **2013**, *61*, 2783−2792.
(37) Kumar, N.; George, B. P. A.; Abrahamse, H.; Parashar, V.; Ray, S. S.; Ngila, J. C. A Novel Approach to Low-Temperature Synthesis of Cubic HfO_2 Nanostructures and Their Cytotoxicity. *Sci. Rep.* **2017**, *7*, No. 9351.
(38) Lee, D.; Gao, X.; Fan, L.; Guo, E. J.; Farmer, T. O.; Heller, W. T.; Ward, T. Z.; Eres, G.; Fitzsimmons, M. R.; Chisholm, M. F.; Lee, H. N. Nonequilibrium Synthesis of Highly Porous Single-Crystalline Oxide Nanostructures. *Adv. Mater. Interfaces* **2017**, *4*, No. 1601034.
(39) Zhou, G.; Gorte, R. J. Thermodynamic Investigation of the Redox Properties for Ceria - Hafnia, Ceria - Terbia, and Ceria - Praseodymia Solid Solutions. *J. Phys. Chem. B* **2008**, *112*, 9869−9875.
(40) Shiraishi, T.; Choi, S.; Kiguchi, T.; Shimizu, T.; Funakubo, H.; Konno, T. J. Formation of the Orthorhombic Phase in CeO_2-HfO_2 Solid Solution Epitaxial Thin Films and Their Ferroelectric Properties. *Appl. Phys. Lett.* **2019**, *114*, No. 232902.
(41) Baidya, T.; Hegde, M. S.; Gopalakrishnan, J. Oxygen-Release/Storage Properties of $Ce_{0.5}M_{0.5}O_2$ (M = Zr, Hf) Oxides: Interplay of Crystal Chemistry and Electronic Structure. *J. Phys. Chem. B* **2007**, *111*, 5149−5154.
(42) Chavan, S. V.; Tyagi, A. K. Investigations on Ceria-Hafnia System for Phase Analysis, and HT-XRD Studies on a Few Cubic Compositions. *Mater. Sci. Eng., A* **2006**, *433*, 203−207.
(43) Andrievskaya, E. R.; Gerasimyuk, G. I.; Kornienko, O. A.; Samelyuk, A. V.; Lopato, L. M.; Red'ko, V. P. Phase Equilibria in the System HfO_2-ZrO_2-CeO_2 at 1500 °C. *Powder Metall. Met. Ceram.* **2006**, *45*, 448−456.
(44) Wang, Y.; Wei, F.; Yue, S.; Yang, Z.; Du, J. Epitaxial Growth of HfO_2 Doped CeO_2 Thin Films on Si(001) Substrates for High-κ Application. *Appl. Phys. Lett.* **2008**, *92*, No. 012915.
(45) Raitano, J. M.; Khalid, S.; Marinkovic, N.; Chan, S. W. Nano-Crystals of Cerium-Hafnium Binary Oxide: Their Size-Dependent Structure. *J. Alloys Compd.* **2015**, *644*, 996−1002.
(46) Dou, C.; Kakushima, K.; Ahmet, P.; Tsutsui, K.; Nishiyama, A.; Sugii, N.; Natori, K.; Hattori, T.; Iwai, H. Resistive Switching Behavior of a CeO_2 Based ReRAM Cell Incorporated with Si Buffer Layer. *Microelectron. Reliab.* **2012**, *52*, 688−691.
(47) Kim, G. S.; Song, H.; Lee, Y. K.; Kim, J. H.; Kim, W.; Park, T. H.; Kim, H. J.; Min Kim, K.; Hwang, C. S. Defect-Engineered Electroforming-Free Analog HfO_x Memristor and Its Application to the Neural Network. *ACS Appl. Mater. Interfaces* **2019**, *11*, 47063−47072.
(48) Ali, S.; Bae, J.; Lee, C. H.; Kobayashi, N. P.; Shin, S.; Ali, A. Resistive Switching Device with Highly Asymmetric Current−Voltage Characteristics: A Solution to Backward Sneak Current in Passive Crossbar Arrays. *Nanotechnology* **2018**, *29*, No. 455201.
(49) Dimitrakis, P. *Charge-Trapping Non-Volatile Memories: Volume 2—Emerging Materials and Structures*; Springer International Publishing, 2017; Vol. 2.
(50) Biju, K. P.; Liu, X.; Bourim, E. M.; Kim, I.; Jung, S.; Siddik, M.; Lee, J.; Hwang, H. Asymmetric Bipolar Resistive Switching in Solution-Processed Pt/TiO_2/W Devices. *J. Phys. D: Appl. Phys.* **2010**, *43*, No. 495104.
(51) Yoshida, C.; Yoshida, A.; Tamura, H. Nanoscale Conduction Modulation in Au/Pb(Zr,Ti)O_3/$SrRuO_3$ Heterostructure. *Appl. Phys. Lett.* **1999**, *75*, 1449−1451.
(52) Hölzl, J.; Schulte, F. K. Work Function of Metals. In *Encyclopedia of Interfacial Chemistry: Surface Science and Electrochemistry*; Elsevier, 1979; pp 1−150.
(53) Wang, X.; Cai, C. Resistance Switching Induced by Electric Field and Light Illumination in Device of FTO/CeO_2/Electrolyte/FTO. 2012, arXiv:1210.7558. arXiv.org e-Print archive. http://arxiv.org/abs/1210.7558.
(54) Monaghan, S.; Hurley, P. K.; Cherkaoui, K.; Negara, M. A.; Schenk, A. Determination of Electron Effective Mass and Electron Affinity in HfO_2 Using MOS and MOSFET Structures. *Solid-State Electron.* **2009**, *53*, 438−444.
(55) Lanza, M. A Review on Resistive Switching in High-k Dielectrics: A Nanoscale Point of View Using Conductive Atomic Force Microscope. *Materials* **2014**, *7*, 2155−2182.

https://doi.org/10.1021/acsaelm.1c00791
ACS Appl. Electron. Mater. 2021, 3, 5278−5286